MATERIALS SCIENCE

High–aspect ratio zeolitic imidazolate framework (ZIF) nanoplates for hydrocarbon separation membranes

Ohchan Kwon[1]†, Minsu Kim[1]†, Eunji Choi[1], Jun Hyuk Bae[1], Sungmi Yoo[2], Jong Chan Won[2,3], Yun Ho Kim[2,3], Ju Ho Shin[4], Jong Suk Lee[4], Dae Woo Kim[1]*

Metal-organic frameworks with high aspect ratios have the potential to yield high-performance gas separation membranes. We demonstrate the scalable synthesis of high–aspect ratio zeolitic imidazolate framework (ZIF)–8 nanoplates via a direct template conversion method in which high aspect ratio–layered Zn hydroxide sheets [$Zn_5(NO_3)_2(OH)_8$] were used as the sacrificial precursor. Successful phase conversion occurs as a result of the collaboration of low template stability and delayed delivery of 2-methylimidazole in weakly interacting solvents, particularly using acetone. When the ZIF-8 nanoplates with an average aspect ratio of 20 were shear aligned in the 6FDA-DAM polymer matrix by bar coating, the separation performance for propylene/propane far surpassed that of the previously reported mixed matrix and polymeric membranes, showing a propylene permeability of 164 Barrer and selectivity of 33.4 at 40 weight % loadings.

INTRODUCTION

Realizing high–aspect ratio morphologies in selective materials for gas separation has well-known benefits. Their planar structure allows for the deposition of ultrathin selective layers on permeable substrates, where molecular sieving is achieved either by the atomic pores in the sheet basal planes or by the interlayer spacing between the plates (*1*). Likewise, the incorporation of selective flakes in polymeric membranes also grants additional values. Arising from the alignment of the filler and its improved integration to the polymer phase, these mixed matrix membranes (MMMs) exhibit enhanced selectivity, higher filler loadings, and strengthened mechanical stability (*2*, *3*).

Previously, the aforementioned effects have been best demonstrated by two-dimensional (2D) porous materials, including zeolites, metal-organic frameworks (MOF), graphene, and carbon nitride (*4*–*7*). Among these, MOFs and zeolites effectively achieve high selectivity of various gases owing to their densely populated crystalline pores that can be tuned according to the target molecules (*8*). However, only a limited number of intrinsically 2D MOFs and zeolite variants have been reported (*9*, *10*), where the synthesis procedure requires multistep approaches to remove non–ideal-shaped particles, resulting in low yields (*11*). When the separation targets hydrocarbons, such as paraffin/olefin and xylene isomers, only a few 2D materials are available (*7*, *12*). To the best of our knowledge, hydrocarbon-selective MOF nanosheets are yet to be realized, although currently reported 2D MOFs are effective for relatively large–molecular size variances, such as H_2/CO_2 separation [$Zn_2(bim)_4$ and $Zn_2(bim)_3$] and CO_2/CH_4 separation (CuBDC) (*2*, *4*, *13*, *14*).

As an alternative to the direct synthesis of MOF nanosheets, the template-based conversion method offers a practical pathway for preparing hydrocarbon-separating shape-controlled MOFs, including zeolitic imidazolate frameworks (ZIF). The strategy allows the realization of various shapes (nanowire, plate, and spherical particles) in polycrystalline MOF particles resembling the mother template (*15*–*18*). However, high aspect ratio, planar morphologies have not been demonstrated in these instances and are rarely applied for membrane fabrications. Commonly, previous shape-controlled MOF particles had small aspect ratios, which did not translate into notable performance enhancements (*19*) or failed to maintain their unique pore structures (*20*, *21*). In addition, traditional template conversion uses relatively stable or unreactive templates such as metal oxides, which are known to remain as a barrier layer hindering molecular transport (*22*, *23*).

Herein, we demonstrate the scalable synthesis of high–aspect ratio ZIF-8 nanoplates via direct conversion of layered hydroxide nanosheets with a $Zn_5(NO_3)_2(OH)_8$ crystal type. Because of the exploited template's chemistry, the resulting planar ZIF-8 particles had attractive properties for separative applications. Although the structure of the prepared nanoplates is polycrystalline and differs from conventional 2D materials with atomic thickness, they share similar structural benefits with sufficiently high aspect ratios. The produced ZIF-8 nanoplates have an average lateral size of 4 μm and thickness of approximately 200 nm, resulting in an aspect ratio of 20. These were further incorporated into the 6FDA-DAM polymer to fabricate MMMs and were tested for propylene/propane separation. The measured propylene/propane separation performances with the ZIF-8 nanoplate/6FDA-DAM membrane surpassed previously reported MMM results for propylene/propane separation.

RESULTS

Synthesis of ZIF-8 nanoplate via conversion method

Figure 1A provides a schematic of ZIF-8 nanoplate synthesis. Among the various MOF crystals, ZIF-8 was selected owing to its effective aperture size of approximately 4 Å, which is ideal for separating propylene/propane molecules and is the most widely studied MOF for gas separation (*24*–*26*). The ZIF-8 nanoplates are developed by

[1]Department of Chemical and Biomolecular Engineering, Yonsei University, 50 Yonsei-ro, Seodaemun-gu, Seoul 03722, Republic of Korea. [2]Advanced Materials Division, Korea Research Institute of Chemical Technology, 141 Gajeong-ro, Yuseong-gu, Daejeon 34114, Republic of Korea. [3]Advanced Materials and Chemical Engineering, KRICT School, University of Science and Technology, 217 Gajeong-ro, Yuseong-gu, Daejeon 34114, Republic of Korea. [4]Department of Chemical and Biomolecular Engineering, Sogang University, 35 Baekbeom-ro, Mapo-gu, Seoul 04107, Republic of Korea.
*Corresponding author. Email: audw1105@yonsei.ac.kr
†These authors contributed equally to this work.

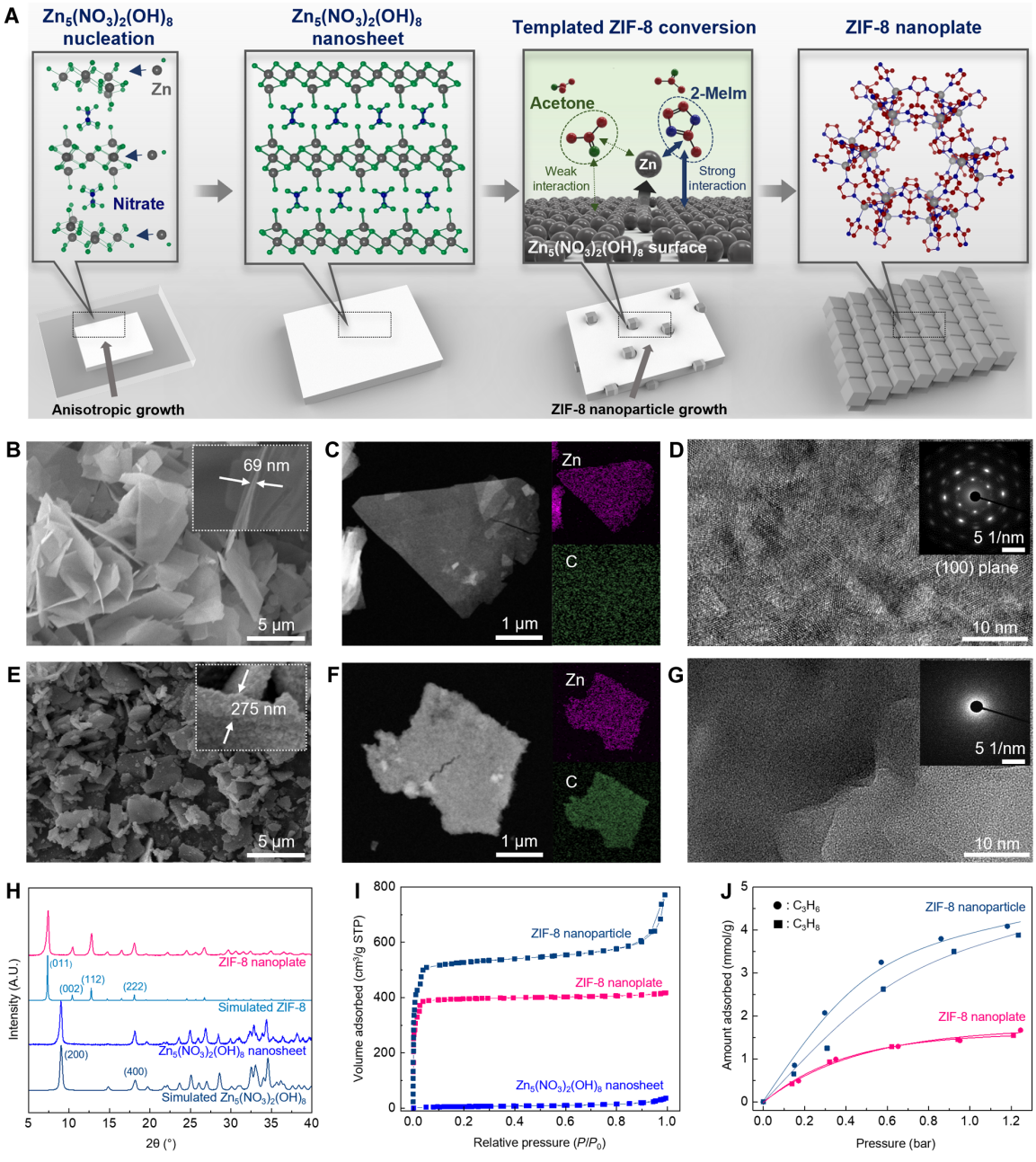

Fig. 1. Synthesis and characterizations of ZIF-8 nanoplates. (**A**) Schematic illustration of ZIF-8 nanoplate synthesis from $Zn_5(NO_3)_2(OH)_8$ nanosheet. 2-MeIm, 2-methylimidazole. (**B** and **E**) Scanning electron microscopy (SEM) images of $Zn_5(NO_3)_2(OH)_8$ and ZIF-8 nanoplate. (**C** and **F**) Scanning transmission electron microscopy (STEM) images of $Zn_5(NO_3)_2(OH)_8$ and ZIF-8 nanoplate and corresponding energy-dispersive spectroscopy (EDS) mapping images. (**D** and **G**) High-resolution TEM images of basal plane of $Zn_5(NO_3)_2(OH)_8$ and ZIF-8 nanoplate. Insets: Selected-area electron diffraction patterns obtained from the location of the TEM images. (**H**) XRD patterns of $Zn_5(NO_3)_2(OH)_8$ and ZIF-8 nanoplate. A.U., arbitrary unit. (**I**) N_2 adsorption-desorption isotherms measured at 77 K. STP, Standard temperature and pressure. (**J**) C_3H_6/C_3H_8 adsorption isotherms of ZIF-8 nanoparticle and nanoplate measured at room temperature (301 K).

first synthesizing a high–aspect ratio Zn template in the form of $Zn_5(NO_3)_2(OH)_8$. Thereafter, the phase conversion is completed by introducing 2-methylimidazole (2-MeIm) linkers solvated in acetone. Syringe pumps were used to control the injection rate of the reactants, which was critical for maintaining the nanoplate's shape throughout the conversion (fig. S1). Because the aspect ratio of the template determines that of the final ZIF-8 nanoplate, the shape of $Zn_5(NO_3)_2(OH)_8$ was controlled by selecting alkaline ions added during synthesis (fig. S2 and Materials and Methods section). When LiOH was used as the reactant, the $Zn_5(NO_3)_2(OH)_8$ nanosheet yielded the highest lateral length of up to 8 μm.

We emphasize that reported ZnO-based conversion is unsuitable for membrane applications because the conversion only partially occurs on surfaces, and the underlying unconverted ZnO layer hinders

gas permeation (*15*, *16*, *27*). Figure S3 confirms that $Zn_5(NO_3)_2(OH)_8$ has a greater conversion extent than the ZnO template under identical conditions because $Zn_5(NO_3)_2(OH)_8$ has weaker chemical stability than ZnO. Because the phase transition is complete, resulting in a 100% yield, further purification is not required, suggesting the feasibility of scalable synthesis (fig. S4).

Another critical feature of the conversion step is related to the selection of the optimal solvent for 2-MeIm delivery and its injection rate. Because acetone has a weak solvent-template interaction, it minimizes unnecessary template dissolution and aids in the retention of the original morphology (fig. S5). In addition, the ligand injection rate and concentration must be sufficiently controlled to incur a complete phase transition; otherwise, a passivation ZIF-8 layer forms on the surface of $Zn_5(NO_3)_2(OH)_8$ nanosheets and terminates the conversion reaction (fig. S6). To confirm this hypothesis, the morphology of the nanoplates during the conversion process was investigated under selected time intervals (fig. S7). Initially, the ZIF-8 crystals form in localized islands on the surface of the templates, suggesting that slower injection delays the rapid formation of a protective ZIF-8 layer. This behavior is also consistent with the results observed with varying ligand concentrations (fig. S8), where higher 2-MeIm presence allows more extensive coverage of ZIF-8 particles with reduced intercrystallite distances. Therefore, the conversion likely proceeds at the defects between the crystals with exposed template surfaces. Extending the reaction time further facilitates phase transformation by increasing the potential of ligand exposure to the unconverted inner cores.

The scanning electron microscopy (SEM) image and the inset of Fig. 1B show that the synthesized $Zn_5(NO_3)_2(OH)_8$ sheets have an average thickness of 70 nm with an average aspect ratio of 60. The dimensions of the templates were uniform, and single-layer sheets were mainly obtained, while stacked nanosheets with a thickness around 100 nm were occasionally observed. The scanning transmission electron microscopy (STEM) and energy-dispersive spectroscopy (EDS) mapping images in Fig. 1C demonstrate that the template is composed of Zn without C species. The high-resolution TEM (HR-TEM) image depicted in Fig. 1D shows hexagonal lattices intrinsic to the basal planes of $Zn_5(NO_3)_2(OH)_8$, which were further confirmed by the hexagonal selected-area electron diffraction (SAED) pattern obtained from the [100] zone axis.

Figure 1E demonstrates the SEM image of the prepared ZIF-8 nanoplates with a nominal thickness of approximately 275 nm. During the SEM observation at high magnification, we observed thickening of the nanoplate due to electron beam exposure. Therefore, the actual thickness is expected to be in the range of 200 nm, given from the atomic force microscopy measurements (fig. S9), yielding an aspect ratio of approximately 20 (fig. S10). Apart from smaller aspect ratio residues, no isotropic ZIF-8 single crystals were observed, and further processing was not required to separate the nanoplates and undesirable particles. The STEM image presented in Fig. 1F shows that the nanoplate shape was well maintained after the ligand treatment. EDS mapping images depict an even distribution of Zn and C species arising from the organic linkers, indicating the successful and uniform conversion of the template. The high-magnification HR-TEM image shown in Fig. 1G does not reveal any crystalline lattice structures of $Zn_5(NO_3)_2(OH)_8$. Instead, tightly bound individual crystallites with sizes of tens of nanometers can be observed, implying the polycrystalline nature of the ZIF-8 nanoplates. Moreover, the loss of the hexagonal SAED pattern indicates that no precursor phase remained in the through-plane of the nanoplates. The bulk crystalline structures of the $Zn_5(NO_3)_2(OH)_8$ and ZIF-8 nanoplates were confirmed by x-ray diffraction (XRD) (Fig. 1H). The peaks of $Zn_5(NO_3)_2(OH)_8$, including the strongest (200) peak attributed to the layered Zn and OH brucite sheets, are in good agreement with the patterns simulated by JCPDS 24-2460 (*28*, *29*). After the conversion, no peaks related to the template were observed within the product, and only characteristic ZIF-8 patterns were detected, suggesting complete conversion, as confirmed by the TEM images presented in Fig. 1G.

Gas adsorption experiments were performed to investigate the pore structure of the prepared ZIF-8 nanoplates. ZIF-8 nanoparticles were synthesized as references. Figure 1I shows the N_2 isotherms measured at 77 K. Compared to the $Zn_5(NO_3)_2(OH)_8$ template, both ZIF-8 samples display type 1 hysteresis, with an initial sharp increase in the region of low relative pressures ($P/P_0 < 0.1$), indicating micropore formation after phase conversion (*30*). Conversely, in the higher-pressure region ($P/P_0 > 0.8$), a hysteresis corresponding to the interparticle meso/microporosity is apparent in the ZIF-8 nanoparticle sample (*31*). These behaviors are not observed for the ZIF-8 nanoplate sample, implying that crystallites are tightly constrained in the polycrystal matrix without grain-boundary voids, which may allow nonselective permeation. Owing to the nanoplate shape with a lower external surface area, the Brunauer-Emmett-Teller surface area of the ZIF-8 nanoplates was 1244 m^2/g, which is lower than the 1518 m^2/g of ZIF-8 particles. Figure 1J illustrates the propylene/propane adsorption isotherms of the ZIF-8 nanoparticle/plate taken at room temperature conditions. The measured results indicate similar adsorption characteristics between the nanoplates and particles, suggesting that the pore structure and adsorption properties of the ZIF-8 nanoplates were identical to those of the nanoparticles, and the conversion process did not alter the crystal structure.

Fabrication of the ZIF-8 nanoplates/6FDA-DAM MMMs

To demonstrate the benefits of the ZIF-8 nanoplate in enhancing the gas separation performance, we fabricated MMMs by hybridizing with the 6FDA-DAM polymer via bar coating. The selected pair is well known for its propylene/propane separation properties and has been thoroughly studied (*32*–*35*). Furthermore, the vast number of studies using isotropic ZIF-8 particles are advantageous for visualizing the effect of a high aspect ratio on the separation performance. Figure 2A depicts the cross-sectional configurations of the nanoplates incorporated in the polymer matrix with increasing content. The ZIF-8 nanoplates were well dispersed and aligned throughout the polymer phase with decreased interfiller spacing at higher concentrations. Unlike previous isotropic particles, additional surface treatment of the filler was not necessary to ensure the uniform dispersion of the nanoplates in the polymer matrix. Considering that the normal-plane orientation of selective fillers is critical in determining the selectivity of 2D material–based MMMs, bar coating offers a scalable pathway for membrane fabrication with highly aligned fillers owing to the induced shear force (Fig. 2B) (*36*, *37*). The distribution of ZIF-8 nanoplates in the polymer matrix was better portrayed in the EDS mapping analysis of the 40 weight % (wt %) membrane (Fig. 2C). C species were evenly detected throughout the membrane because the element exists in both the ZIF-8 and polymeric phases. On the other hand, Zn species are primarily observed as horizontal filaments coinciding with the location of nanoplates, representing the fillers' generally aligned states. Aggregation of the nanoplates

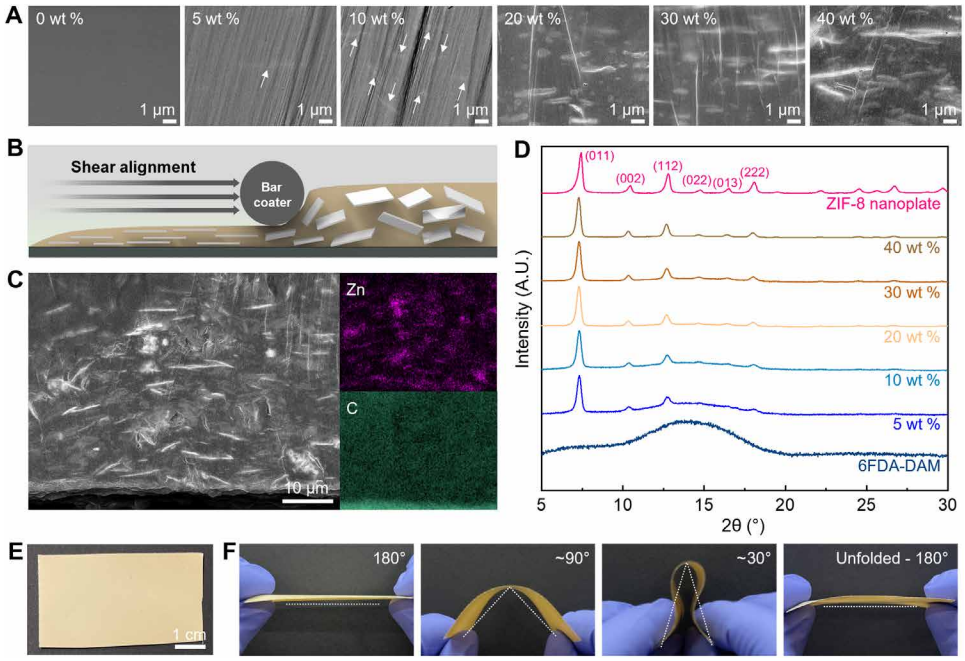

Fig. 2. Structure of ZIF-8 nanoplate/6FDA-DAM membranes. (**A**) Cross-sectional SEM images of the membranes by increasing ZIF-8 nanoplate content. The samples were prepared by using a cross-sectional polisher. The ZIF-8 nanoplates are marked with white arrows. (**B**) Shear-induced alignment mechanism of the ZIF-8 nanoplates during the bar-coating process. (**C**) Cross-sectional SEM image of 40 weight % (wt %) samples with EDS mapping images. (**D**) XRD patterns of the membranes with increasing weight percent of ZIF-8 nanoplates. (**E**) Photographic top-view image of a 40 wt % MMM and (**F**) the corresponding bending images of the membrane under differing angles (30° to 180°) (photo credit: Ohchan Kwon, Yonsei University).

was not observed, indicating the homogeneous distribution. Specifically, we emphasize that the as-prepared ZIF-8 nanoplate can be directly used without further purification and exfoliation processes, commonly required in other 2D MOF and zeolite preparation methods (*9*, *11*).

Figure 2D shows the corresponding XRD patterns of the prepared MMMs. The pristine 6FDA-DAM membrane exhibits a broad, amorphous peak in the region of 10° to 20°. As the ZIF-8 content increases, the peak attributed to the polymer phase is diminished, and the characteristic ZIF-8 peaks are evolved. This sharp increase in the filler peaks indicates that the diffraction occurs primarily because of the ZIF-8 phase, and the coating process does not cause any structural modification of the crystals. Furthermore, we report no evidence of the orientation of the crystallites, which has been previously reported for 2D zeolites and MOFs, suggesting that the nanoplate consists of randomly oriented ZIF-8 polycrystals (*7*). Another aspect to emphasize is the high mechanical durability of the prepared MMMs. Even under severe bending regiments (30° to 180°), the 40 wt % loaded MMM showed fair handleability (Fig. 2, E and F), which is in contrast to the brittle isotropic ZIF-8–loaded MMMs with relatively lower concentrations (30 wt %; fig. S11). This observation reveals that incorporating fillers with high aspect ratios can improve both the mechanical properties of MMMs and the gas separation performances. The actual separation properties of the membrane after the bending tests are discussed in the following section.

C_3H_6/C_3H_8 separation performance

The propylene/propane separation performance of the membrane was measured under both single-gas and mixed-gas conditions. Figure 3A and fig. S12 show the selectivity and permeability of MMMs with an increasing amount of ZIF-8 nanoplates up to 40 wt %, plotted against previously reported mixed-gas, single-gas, and MMM upper bounds (*34*, *38*–*41*). The average thickness of the freestanding MMM was approximately 45 μm and was tested without using a support layer. The single-gas propylene permeability and propylene/propane selectivity of the pristine 6FDA-DAM membrane were measured at 44.8 Barrer and 9.3, respectively, which is consistent with previous studies (*41*–*43*). The addition of 5 wt % ZIF-8 nanoplates increased the permeability and selectivity to 77.0 Barrer and 11.4, respectively, which can ultimately be increased to 164.0 Barrer and 33.4 at 40 wt % filler content. For the mixed-gas separation test, the pristine polymer membrane initially exhibited a propylene permeability and propylene/propane selectivity of 25.0 Barrer and 6.5, respectively. At 5 wt % filler content, the permeability and selectivity were enhanced to 40.2 Barrer and 8.1, respectively, which were eventually elevated to 118.2 Barrer and 26.2 with the 40 wt % membrane.

The mixed-gas separation performance was slightly lower than the single-gas test results, which could be attributed to the competitive adsorption of propylene and propane and the plasticization effect (*44*). Despite this minor decrease, the performance of the membrane was the highest among all reported examples (Fig. 3A and table S1). Compared to studies using isotropic ZIF-8 particles (*32*, *40*), our membrane shows superior performances, even with lower filler concentrations, advocating the high–aspect ratio effect of the nanoplates. Moreover, the trend lines of both single- and mixed-gas separation data converge toward the intrinsic separation performance of neat ZIF-8 membranes, denoted by the upper-right purple region in Fig. 3A (*27*, *45*–*49*). This indicates that the performance enhancement is primarily related to the aligned nanoplates providing sufficient selective-layer coverage inside the polymer matrix. MMMs

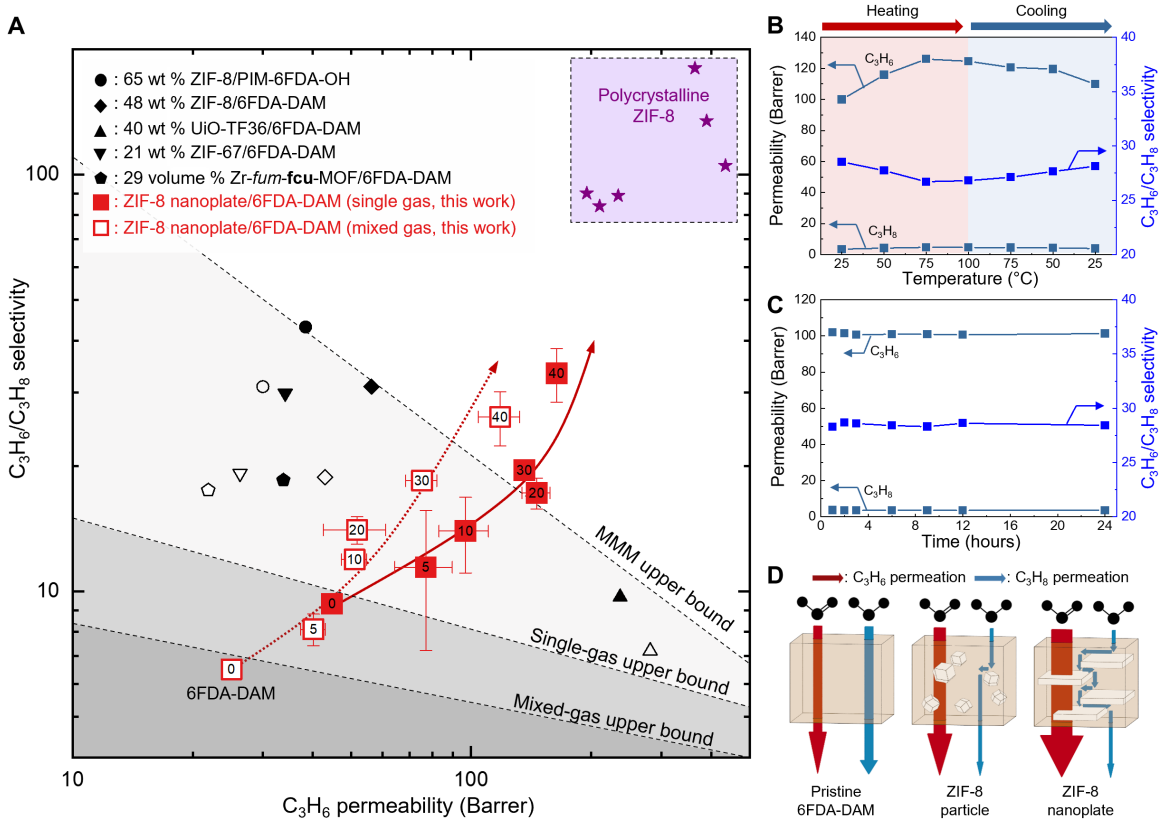

Fig. 3. C_3H_6/C_3H_8 separation performance of the ZIF-8 nanoplate/6FDA-DAM membranes. (**A**) C_3H_6/C_3H_8 separation performance of ZIF-8 nanoplate/6FDA-DAM membranes compared with reported MMMs. Open and closed symbols denote mixed-gas separation and ideal separation values, respectively. (**B**) Separation performance of 40 wt % membrane with varying temperature. (**C**) Twenty-four-hour continuous separation performance tested with the 40 wt % membrane. For both (B) and (C), membranes were tested at 1 bar with a binary mixture. (**D**) Gas permeation mechanism of membranes depending on the filler shape.

above 40 wt % were not reproducible under our experimental conditions, suggesting that an advanced coating method is required for higher loadings, which may enhance the separative characteristics.

The separation performance of the 40 wt % membrane was further tested at various temperatures with binary gas (Fig. 3B). The initial operating temperature was 25°C, and the sample was heated to 100°C. The propylene permeability increased from 100.0 Barrer to 125.0 Barrer, while the propylene/propane selectivity slightly decreased from 28.5 to 26.8. This reduction can be attributed to the increase in the diffusivity of gas molecules at higher temperatures, particularly for propane (*50*). After the heating step, the membrane was restored to its original temperature of 25°C. The measured propylene permeability and selectivity were 109.8 Barrer and 28.1, respectively, which is within a 10% variance from the initial data. In addition, 24-hour continuous separation performance tests were conducted with a 40 wt % membrane under 1 bar, room temperature, and binary gas conditions (Fig. 3C). The membrane showed no evident performance degradation even after 24 hours of continuous operation. A collective assessment of both results indicated the stable nature of the ZIF-8 nanoplate/6FDA-DAM membranes in practical situations.

The MMMs were further tested at 2 bar, binary mixed-gas conditions (fig. S13). The propylene permeability of the 40 wt % MMM decreased to 116.2 Barrer, and the selectivity had slightly reduced to 24.6. However, no marked changes in permeability and selectivity were observed regardless of the nanoplate concentration. Thus, the membranes' overall performance was maintained even under pressure-driven conditions. We note that the tested pressure is lower than practical propylene/propane separations, and additional studies are needed. In addition, the 40 wt % MMM's separation performance after aging (in air, room temperature, 10 days) was observed to be moderately stable with a slight reduction in permeability (fig. S14). We further examined the mechanical durability of the 40 wt % MMM by performing gas separation tests (fig. S15) with the bend-stressed membrane (Fig. 2E). Even after severe flexing cycles, SEM images reveal no discernable difference, and only a slight selectivity decrease was seen because of the physical robustness of the ZIF-8 nanoplate/6FDA-DAM membrane (26.2 to 21.7).

Figure 3D is a model representation depicting the influence of the ZIF-8 fillers on the transport pathway of the 6FDA-DAM polymeric membrane. The sieving properties of ZIF-8 arise because of the varying transport resistance of the gases, where fast-passage propylene molecules are permitted through the crystals, while propane permeation is hindered because of the 4 Å aperture size, which is smaller than the kinetic diameter of propane (4.3 Å) (*24*, *51*, *52*). Therefore, ZIF-8–containing MMMs show better separation performance than pristine 6FDA-DAM membranes. These effects are maximized with horizontally oriented, high–aspect ratio ZIF-8 nanoplates because they provide faster through-plane propylene pathways, while the propane transport resistances are severed because of the increased in-plane tortuosity.

For the theoretical validation of the ZIF-8 filler shape effects, the modified Cussler model was used, which is a mathematical approach describing the transport behaviors in 2D-filler–incorporated MMMs (*53*–*56*). The model is based on the assumption that the selective fillers are perfectly aligned normal to the permeation direction without any interfacial voids inside the polymeric phase. Further details of the calculation and the model are provided in the Materials and Methods section. Here, 20 was selected as the aspect ratio of interest, given that the prepared nanoplate's aspect ratio was approximately 20 (fig. S10).

The Cussler model predicts that increasing the aspect ratio from 1 to 20 results in a substantial propylene/propane selectivity improvement, primarily due to decreased propane flux (fig. S16). This assumption is confirmed by the gas permeation of MMMs with results with varying ZIF-8 aspect ratios. The separation performances are greatly enhanced with higher–aspect ratio fillers (fig. S17), where the selectivity of MMMs with aspect ratio 20 is more than 50% higher than the isotropic particle MMMs. The Cussler model also expects no notable improvement in 6FDA-DAM's selectivity would be seen, even with higher aspect ratios, due to the enhancement being saturated (fig. S18). However, it should be noted that fillers with greater aspect ratios are desirable for preparing ultrathin selective layers and warrant future investigations.

Figure 4 displays the fitting of the simulated data given from the modified Cussler model with both single- and mixed-gas experimental values in Fig. 3A. The blue/red lines of Fig. 4A (single gas) and Fig. 4B (mixed gas) show the theoretical propylene/propane permeability, and the square symbols denote the experimentally measured data. Within the tested MMMs, the propylene permeability was markedly enhanced with higher ZIF-8 nanoplate loading, while the propane permeability was suppressed. The gas permeabilities of both propylene and propane are higher than the calculated expectations, while the enhancement is more pronounced with propylene. Taking the 40 wt % MMM as an example, which had the highest degree of divergence, propylene/propane permeabilities are 109 and 37% higher than the calculated estimates for the single-gas results (Fig. 4A) and 178 and 86% higher in mixed-gas conditions (Fig. 4B). Despite the variances, as the filler concentration increases from 5 to 40 wt %, the propane permeability of both single/mixed-gas experimental results exhibits a reducing trend (32 and 9% reduction for single- and mixed-gas results, respectively). This decreasing tendency is consistent with the Cussler model, indicating the hindered transport of propane due to the planar and selective fillers.

The experimental selectivity of MMMs depending on the ZIF-8 nanoplate concentration was also fitted (Fig. 4, C and D). Calculated selectivity from the model was obtained by the permeability ratio in Fig. 4 (A and B). For both single- and mixed-gas conditions, the selectivity increase was proportional to the ZIF-8 nanoplate concentrations. The values were particularly enhanced with higher filler loadings, which surpassed the expected values calculated by the model (55% higher for both single- and mixed-gas results, 40 wt % MMM). When analyzing the gas permeabilities in Fig. 4 (A and B), the selectivity enhancement is mainly attributed to the promoted propylene permeability collaborating with the slightly reduced

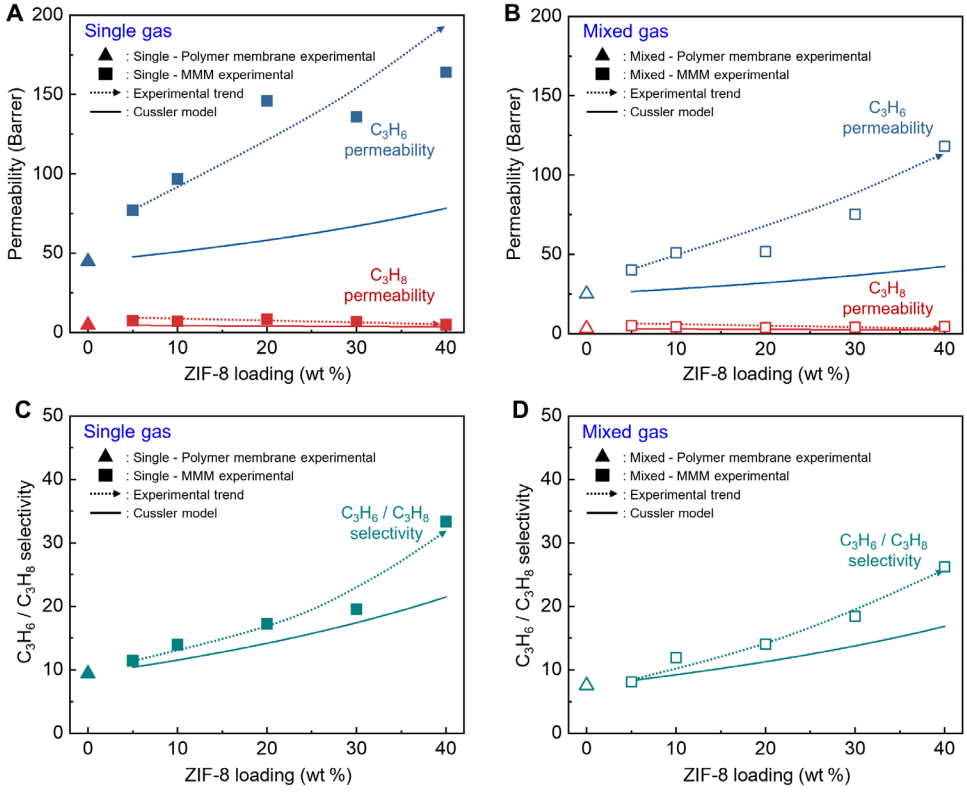

Fig. 4. Comparison of the experimental C_3H_6/C_3H_8 single- and mixed-gas separation results with the modified Cussler model. Comparison of C_3H_6 and C_3H_8 permeability for single gas (**A**) and for mixed gas (**B**). C_3H_6/C_3H_8 selectivity for single gas (**C**) and for mixed gas (**D**). Closed/open squares, respectively, denote single/mixed experimental data points, and the line represents the calculated data from the model. The aspect ratio of the filler used in the model calculation is 20.

propane permeability. This aspect is further demonstrated with the high diffusivity selectivity of the presented 40 wt % ZIF-8 nanoplate/6FDA-DAM membrane where the diffusivity for propylene is increased, while the propane diffusivity is decreased when comparing with reported works (fig. S19).

The exact reasons for the discrepancy between the experimental and simulated values are not well defined. However, the structure of the ZIF-8 nanoplate/6FDA-DAM membrane deviating from the Cussler model assumptions could be one of the possible factors. In the prepared MMMs, despite having an overall horizontal orientation, the nanoplates are not perfectly aligned with some angular variations for individual plates (Fig. 2B). Therefore, the "in-plane" propylene permeation through the loosely aligned fillers may increase the "through-plane" membrane propylene permeation. In addition, nonselective defective voids (*57*–*60*), known to be inherent with MMMs, may exist because no additional surface treatment increasing the filler-polymer interaction was conducted.

DISCUSSION

The current work reports the synthesis of high–aspect ratio ZIF-8 nanoplates for fabricating propylene/propane separation membranes. The phase conversion of the high–aspect ratio $Zn_5(NO_3)_2(OH)_8$ templates determined the sheet-like morphology of the ZIF-8 flakes, and the low stability of the template phase was exploited to enhance the extent of conversion. For the phase conversion, the weak interaction of acetone with the template phase suppresses unnecessary template leaching, which is critical in maintaining the template structure. The produced ZIF-8 nanoplates were molded into MMMs with the 6FDA-DAM polymer by a facile bar–coating method. The induced shear force of the fabrication process achieved in-plane alignment of the nanoplates, which improved the separation performance. The obtained data were further confirmed by mathematical analysis using the modified Cussler model. To the best of our knowledge, the 40 wt % sample is the highest-functioning MMM for propylene/propane separation reported to date. We believe that our approach can be extended to the preparation of various high–aspect ratio ZIF-type MOF nanoplates for attaining high-performance MMMs for gas separation.

MATERIALS AND METHODS

Synthesis of $Zn_5(NO_3)_2(OH)_8$ nanosheets

A total of 0.02 mol (5.9498 g) of zinc nitrate hexahydrate [$Zn(NO_3)_2{\cdot}6H_2O$, 98%; Sigma-Aldrich] and 0.01 mol (0.4198 g) of lithium hydroxide monohydrate ($LiOH{\cdot}H_2O$, ≥98%; Sigma-Aldrich] were dissolved in 100 and 50 ml of deionized (DI) water. The LiOH DI water solution was slowly injected into the $Zn(NO_3)_2$ solution for 4 hours (12.5 ml/hour) and further stirred for 4 hours. The white precipitates were collected from the mixed solution through vacuum filtration on a polyethersulfone substrate (0.2-μm pore diameter; GVS). The collected precipitates were washed with DI water three times and dried at 20°C in a vacuum oven overnight. Last, $Zn_5(NO_3)_2(OH)_8$ nanosheets were synthesized.

Conversion of $Zn_5(NO_3)_2(OH)_8$ nanosheets to ZIF-8 nanoplates

$Zn_5(NO_3)_2(OH)_8$ nanosheets (0.12 g) were dispersed in 50 ml of acetone (CH_3COCH_3, extra pure, Duksan). A total of 0.02 mol (1.8 g) of 2-MeIm ($CH_3C_3H_2N_2H$, 99.0%; Sigma-Aldrich) was dissolved in 100 ml of acetone. The 2-MeIm acetone solution was slowly injected into the $Zn_5(NO_3)_2(OH)_8$ nanosheet dispersion for 12 hours (8.33 ml/hour) and stirred for 20 hours. The white precipitate was collected from the mixed dispersion through vacuum filtration on a nylon substrate (0.2-μm pore diameter, Sterlitech). The collected precipitates were washed with acetone three times and dried at room temperature in a vacuum oven overnight.

Synthesis of isotropic ZIF-8 particles

Isotropic ZIF-8 particles were synthesized using conventional solvent-based methods. First, 1.4 g of zinc nitrate hexahydrate was dissolved in 100 ml of methanol (CH_3OH, GR, Duksan), and in a separate batch, 1.4 g of 2-MeIm was also dissolved in 100 ml of methanol. Two reactants were immediately mixed under heavy stirring for 1 hour at 25°C. The yielded white precipitate was collected using a centrifuge and washed with methanol several times. Last, the collected ZIF-8 powder was dried in a 60°C vacuum for at least 24 hours.

Fabrication of pristine 6FDA-DAM membranes

6FDA-DAM was dissolved in *N*-methyl-2-pyrrolidone (NMP) to form a 15 wt % solution. The solution was stirred for 24 hours to dissolve the polymer fully. A pure 6FDA-DAM dense film was formed on a clean glass plate by casting the solution with a bar coater (Yoshimitsu, YBA-7). The cast membrane was immediately moved to a vacuum oven and dried at 80°C for 1 hour, 100°C for 1 hour, 120°C for 1 hour, and 200°C for 16 hour under vacuum. The film was peeled off from the glass plate and further dried in a vacuum oven at 60°C overnight prior to the gas permeation test to remove any residual solvent.

Fabrication of ZIF-8 nanoplate/6FDA-DAM membranes

A dope solution was prepared separately to prevent agglomeration of the powder. 6FDA-DAM polymer with a molecular weight of 240,000 Da, obtained from the Korea Research Institute of Chemical Technology, was dissolved in NMP (extra pure, Daejung) to form a 20 wt % solution. In a separate vial, ZIF-8 nanoplates with different loadings and small amounts of 6FDA-DAM were dissolved in NMP to fit a 15 wt % solution. Each solution was stirred for 24 hours to dissolve the polymer. The two solutions were then mixed and stirred for another 24 hours. ZIF-8 nanoplate/6FDA-DAM membrane was formed on a clean glass plate by casting the solution with a bar coater. The casted membrane was immediately moved to a vacuum oven and dried at 80°C for 1 hour, 100°C for 1 hour, 120°C for 1 hour, and 200°C for 16 hour under vacuum. The film was peeled off from the glass plate and further dried in a vacuum oven at 60°C overnight before the gas permeation test to remove any residual solvent. The fabricated membranes had thicknesses in the range of 32 to 61 μm.

Gas permeation measurements

For the gas permeation tests, membranes were mounted on a stainless steel plain washer. Ni mesh (50 mesh) was used as a supporting layer, which was securely anchored on the washer with an impermeable cellophane tape. Then, the membrane was placed above the mesh, and the edges were sealed with epoxy resin. The area of the tested membranes was approximately 1.4 cm^2. Gas permeation tests were performed using the Wicke-Kallenbach technique. For single-gas measurements, mass flow controllers were used to fix the total

feed flow at 20 ml/min. On the permeate side of the membrane, N_2 was used as a sweep gas flowing at 40 ml/min and was directly injected into the gas chromatograph. For the mixed-gas measurements, a binary gas mixture (50:50) of C_3H_6/C_3H_8 was used. The N_2 sweep gas also flowed at 40 ml/min, while the component gas flowed at 20 ml/min. The composition of the mixed gas on the sweep side of the membrane was analyzed using gas chromatography (YL 6500 GC, YoungIn Chromass). Before the gas concentration on the permeate side was measured by gas chromatography, a minimum equilibration time of 1 hour was applied. The permeability and selectivity were calculated using Eqs. 1 and 2, respectively

$$P_i = \frac{N_i \times l}{\mathrm{A} \times \Delta \mathrm{P}} \quad (1)$$

where P_i is the permeability of the penetrant i, N_i is the molar flow rate of the gas (mol/s), l is the thickness of the membrane, A is the effective area of the membrane (m^2), and ΔP is the pressure difference between the feed and sweep sides (Pa)

$$\alpha_{i/j} = \frac{P_i}{P_j} \quad (2)$$

where P_i and P_j denote the permeabilities of penetrants i and j. The ideal selectivity was calculated from the single-gas permeabilities, and the mixture selectivity was calculated from the permeabilities of the binary mixture. The reproducibility of the gas permeation performance data was tested with several batches of parallelly fabricated membranes, and the error-bar spread is calculated by the SD from more than three samples.

Membrane performance estimation by modified Cussler model

Several models have been suggested to explain the transport mechanisms of membranes filled with semipermeable flakes. The modified Cussler model is a mathematical model that considers diffusion through an oriented, staggered array of 2D flakes embedded in a continuous polymer matrix (*56*). This model describes 2D transport in mixed-matrix membranes with an aspect ratio α and volume fraction ϕ of the filler, as shown in Eq. 3

$$P_i^{\mathrm{C}} = \frac{P_i^{\mathrm{M}}}{(1-\phi) + \frac{1}{\left[\left(\frac{1}{\phi}\right)\left(\frac{P_i^{\mathrm{F}}}{P_i^{\mathrm{M}}}\right) + \left(\frac{(1-\phi)}{\alpha^2\phi^2}\right)\right]}} \quad (3)$$

P_i^{C} represents the permeability of component i in a mixed-matrix membrane; P_i^{M} is the permeability of component i in the polymer matrix; and P_i^{F} is the permeability of component i in the filler material, which is the incorporated ZIF-8 nanoplates in this work. The single-gas permeability values of ZIF-8 used for the model calculation were 390 Barrer for propylene and 2.9 Barrer for propane (*45*). For the mixed-gas propylene and propane permeability values, 166.3 and 1.92 Barrer were used (*61*). The propylene/propane permeabilities of 6FDA-DAM were experimentally obtained as 44.8/4.76 Barrer for single-gas measurement and 25.0/3.32 Barrer for mixed-gas measurement, respectively. To calculate the volume fraction of the ZIF-8 nanoplates, 0.95 and 1.3342 g/cm^3 were used as the densities of ZIF-8 and 6FDA-DAM, respectively (*62*, *63*).

Characterization

SEM images and the corresponding elemental mapping images were obtained using a field emission SEM (JEOL, 7800F) equipped with an EDS probe and AZtecEnergy analysis software (Oxford Instruments). All HR-TEM, SAED, STEM, and EDS images were obtained using Cs-corrected JEM-ARM200F equipment. XRD patterns were obtained using a high-resolution diffractometer (SmartLab, Rigaku, Cu K radiation, λ = 1.54 Å). N_2 adsorption-desorption isotherms (77 K) were measured using a BELSORP-mini II instrument (BEL Japan). Equilibrium sorption isotherms of C_3H_6 and C_3H_8 for the ZIF-8 nanoparticles/plate were evaluated using the pressure decay method at 301 K. Diffusivity and the solubility coefficients of the 40 wt % membrane were also derived from the similarly measured sorption isotherms (*64*).

SUPPLEMENTARY MATERIALS

Supplementary material for this article is available at https://science.org/doi/10.1126/sciadv.abl6841

REFERENCES AND NOTES

1. L. Cheng, G. Liu, J. Zhao, W. Jin, Two-dimensional-material membranes: Manipulating the transport pathway for molecular separation. *Acc. Mater. Res.* **2**, 114–128 (2021).
2. T. Rodenas, I. Luz, G. Prieto, B. Seoane, H. Miro, A. Corma, F. Kapteijn, F. X. Llabrés i Xamena, J. Gascon, Metal–organic framework nanosheets in polymer composite materials for gas separation. *Nat. Mater.* **14**, 48–55 (2015).
3. Y. Yang, K. Goh, R. Wang, T.-H. Bae, High-performance nanocomposite membranes realized by efficient molecular sieving with CuBDC nanosheets. *Chem. Commun.* **53**, 4254–4257 (2017).
4. Y. Peng, Y. Li, Y. Ban, H. Jin, W. Jiao, X. Liu, W. Yang, Metal-organic framework nanosheets as building blocks for molecular sieving membranes. *Science* **346**, 1356–1359 (2014).
5. S. P. Koenig, L. Wang, J. Pellegrino, J. S. Bunch, Selective molecular sieving through porous graphene. *Nat. Nanotechnol.* **7**, 728–732 (2012).
6. Y. Wang, B. Gao, Q. Yue, Z. Wang, Graphitic carbon nitride (g-C3N4)-based membranes for advanced separation. *J. Mater. Chem. A* **8**, 19133–19155 (2020).
7. P. Kumar, D. W. Kim, N. Rangnekar, H. Xu, E. O. Fetisov, S. Ghosh, H. Zhang, Q. Xiao, M. Shete, J. I. Siepmann, T. Dumitrica, B. McCool, M. Tsapatsis, K. A. Mkhoyan, One-dimensional intergrowths in two-dimensional zeolite nanosheets and their effect on ultra-selective transport. *Nat. Mater.* **19**, 443–449 (2020).
8. J. Liang, Z. Liang, R. Zou, Y. Zhao, Heterogeneous catalysis in zeolites, mesoporous silica, and metal–organic frameworks. *Adv. Mater.* **29**, 1701139 (2017).
9. M. Zhao, Y. Huang, Y. Peng, Z. Huang, Q. Ma, H. Zhang, Two-dimensional metal–organic framework nanosheets: Synthesis and applications. *Chem. Soc. Rev.* **47**, 6267–6295 (2018).
10. W. J. Roth, P. Nachtigall, R. E. Morris, J. Cejka, Two-dimensional zeolites: Current status and perspectives. *Chem. Rev.* **114**, 4807–4837 (2014).
11. M. Dakhchoune, L. F. Villalobos, R. Semino, L. Liu, M. Rezaei, P. Schouwink, C. E. Avalos, P. Baade, V. Wood, Y. Han, M. Ceriotti, K. V. Agrawal, Gas-sieving zeolitic membranes fabricated by condensation of precursor nanosheets. *Nat. Mater.* **20**, 362–369 (2021).
12. M. Y. Jeon, D. Kim, P. Kumar, P. S. Lee, N. Rangnekar, P. Bai, M. Shete, B. Elyassi, H. S. Lee, K. Narasimharao, S. N. Basahal, S. Al-Thabaiti, W. Xu, H. J. Cho, E. O. Fetisov, R. Thayaparajan, R. F. Bejaco, W. Fan, K. A. Mkhoyan, J. I. Siepmann, M. Tsapatsis, Ultra-selective high-flux membranes from directly synthesized zeolite nanosheets. *Nature* **543**, 690–694 (2017).
13. X. Wang, C. Chi, K. Zhang, Y. Qian, K. M. Gupta, Z. Kang, J. Jiang, D. Zhao, Reversed thermo-switchable molecular sieving membranes composed of two-dimensional metal-organic nanosheets for gas separation. *Nat. Commun.* **8**, 14460 (2017).
14. Y. Peng, Y. Li, Y. Ban, W. Yang, Two-dimensional metal–organic framework nanosheets for membrane-based gas separation. *Angew. Chem. Int. Ed.* **129**, 9889–9893 (2017).
15. X. Wang, J. Liu, S. Leong, X. Lin, J. Wei, B. Kong, Y. Xu, Z.-X. Low, J. Yao, H. Wang, Rapid construction of ZnO@ ZIF-8 heterostructures with size-selective photocatalysis properties. *ACS Appl. Mater. Interfaces* **8**, 9080–9087 (2016).
16. M.-K. Kim, D. Kim, J. Y. Seo, O. Buyukcakir, A. Coskun, Nanostructured ZnO as a structural template for the growth of ZIF-8 with tunable hierarchical porosity for CO_2 conversion. *CrstEngComm* **19**, 4147–4151 (2017).
17. C. Keum, H. Lee, C. Kwon, B. Han, S.-Y. Lee, Metal-induced self-assembly template for controlled growth of ZIF-8 nanorods. *Chem. Mater.* **32**, 7941–7950 (2020).
18. J. Meng, X. Liu, C. Niu, Q. Pang, J. Li, F. Liu, Z. Liu, L. Mai, Advances in metal–organic framework coatings: Versatile synthesis and broad applications. *Chem. Soc. Rev.* **49**, 3142–3186 (2020).
19. F. Yang, H. Mu, C. Wang, L. Xiang, K. X. Yao, L. Liu, Y. Yang, Y. Han, Y. Li, Y. Pan, Morphological map of ZIF-8 crystals with five distinctive shapes: Feature of filler

in mixed-matrix membranes on C_3H_6/C_3H_8 separation. *Chem. Mater.* **30**, 3467–3473 (2018).
20. Z.-X. Low, J. Yao, Q. Liu, M. He, Z. Wang, A. K. Suresh, J. Bellare, H. Wang, Crystal transformation in zeolitic-imidazolate framework. *Cryst. Growth Des.* **14**, 6589–6598 (2014).
21. Q. Luo, Z. Ding, H. Sun, Z. Cheng, N. Shi, C. Song, M. Han, D. Gu, M. Yi, Y. Sun, L. Xie, W. Huang, A small molecule with a big scissoring effect: Sodium dodecyl sulfate working on two-dimensional metal–organic frameworks. *CrstEngComm* **23**, 1360–1365 (2021).
22. Y. Hu, J. Wei, Y. Liang, H. Zhang, X. Zhang, W. Shen, H. Wang, Zeolitic imidazolate framework/graphene oxide hybrid nanosheets as seeds for the growth of ultrathin molecular sieving membranes. *Angew. Chem. Int. Ed.* **128**, 2088–2092 (2016).
23. P.-F. Liu, K. Tao, G.-C. Li, M.-K. Wu, S.-R. Zhu, F.-Y. Yi, W.-N. Zhao, L. Han, In situ growth of ZIF-8 nanocrystals on layered double hydroxide nanosheets for enhanced CO_2 capture. *Dalton Trans.* **45**, 12632–12635 (2016).
24. E. Choi, S. J. Hong, Y. J. Kim, S. E. Choi, Y. Choi, J. H. Kim, J. Kang, O. Kwon, K. Eum, B. Han, D. W. Kim, Pore tuning of metal-organic framework membrane anchored on graphene-oxide nanoribbon. *Adv. Funct. Mater.* **31**, 2011146 (2021).
25. Z. Lai, Development of ZIF-8 membranes: Opportunities and challenges for commercial applications. *Curr. Opin. Chem. Eng.* **20**, 78–85 (2018).
26. X. Gong, Y. Wang, T. Kuang, ZIF-8-based membranes for carbon dioxide capture and separation. *ACS Sustainable Chem. Eng.* **5**, 11204–11214 (2017).
27. J. H. Lee, D. Kim, H. Shin, S. J. Yoo, H. T. Kwon, J. Kim, Zeolitic imidazolate framework ZIF-8 films by ZnO to ZIF-8 conversion and their usage as seed layers for propylene-selective ZIF-8 membranes. *J. Ind. Eng. Chem.* **72**, 374–379 (2019).
28. W. Stählin, H. R. Oswald, The crystal structure of zinc hydroxide nitrate, $Zn_5(OH)_8(NO_3)_2.2H_2O$. *Acta Crystallogr. B Struct. Crystallogr. Cryst. Chem.* **26**, 860–863 (1970).
29. P. Li, Z. P. Xu, M. A. Hampton, D. T. Vu, L. Huang, V. Rudolph, A. V. Nguyen, Control preparation of zinc hydroxide nitrate nanocrystals and examination of the chemical and structural stability. *J. Phys. Chem. C* **116**, 10325–10332 (2012).
30. F. J. Sotomayor, K. A. Cychosz, M. Thommes, Characterization of micro/mesoporous materials by physisorption: Concepts and case studies. *Acc. Mater. Surf. Res.* **3**, 34–50 (2018).
31. Y. Zhang, Y. Jia, M. LiL. a. Hou, Influence of the 2-methylimidazole/zinc nitrate hexahydrate molar ratio on the synthesis of zeolitic imidazolate framework-8 crystals at room temperature. *Sci. Rep.* **8**, 9597 (2018).
32. C. Zhang, Y. Dai, J. R. Johnson, O. Karvan, W. J. Koros, High performance ZIF-8/6FDA-DAM mixed matrix membrane for propylene/propane separations. *J. Membr. Sci.* **389**, 34–42 (2012).
33. M. Askari, T.-S. Chung, Natural gas purification and olefin/paraffin separation using thermal cross-linkable co-polyimide/ZIF-8 mixed matrix membranes. *J. Membr. Sci.* **444**, 173–183 (2013).
34. H. An, S. Park, H. T. Kwon, H.-K. Jeong, J. S. Lee, A new superior competitor for exceptional propylene/propane separations: ZIF-67 containing mixed matrix membranes. *J. Membr. Sci.* **526**, 367–376 (2017).
35. J. W. Oh, K. Y. Cho, M.-Y. Kan, H. J. Yu, D.-Y. Kang, J. S. Lee, High-flux mixed matrix membranes containing bimetallic zeolitic imidazole framework-8 for C_3H_6/C_3H_8 separation. *J. Membr. Sci.* **596**, 117735 (2020).
36. O. Kwon, Y. Choi, E. Choi, M. Kim, Y. C. Woo, D. W. Kim, Fabrication techniques for graphene oxide-based molecular separation membranes: Towards industrial application. *Nanomaterials* **11**, 757 (2021).
37. A. Akbari, P. Sheath, S. T. Martin, D. B. Shinde, M. Shaibani, P. C. Banerjee, R. Tkacz, D. Bhattacharyya, M. Majumder, Large-area graphene-based nanofiltration membranes by shear alignment of discotic nematic liquid crystals of graphene oxide. *Nat. Commun.* **7**, 10891 (2016).
38. T. H. Lee, J. G. Jung, Y. J. Kim, J. S. Roh, H. W. Yoon, B. S. Ghanem, H. W. Kim, Y. H. Cho, I. Pinnau, H. B. Park, Defect engineering in metal–organic frameworks towards advanced mixed matrix membranes for efficient propylene/propane separation. *Angew. Chem., Int. Ed.* **133**, 13191–13198 (2021).
39. Y. Liu, Z. Chen, G. Liu, Y. Belmabkhout, K. Adil, M. Eddaoudi, W. Koros, Conformation-controlled molecular sieving effects for membrane-based propylene/propane separation. *Adv. Mater.* **31**, 1807513 (2019).
40. X. Ma, R. J. Swaidan, Y. Wang, C.-e. Hsiung, Y. Han, I. Pinnau, Highly compatible hydroxyl-functionalized microporous polyimide-ZIF-8 mixed matrix membranes for energy efficient propylene/propane separation. *ACS Appl. Nano Mater.* **1**, 3541–3547 (2018).
41. R. L. Burns, W. J. Koros, Defining the challenges for C_3H_6/C_3H_8 separation using polymeric membranes. *J. Membr. Sci.* **211**, 299–309 (2003).
42. F. Moghadam, T. H. Lee, I. Park, H. B. Park, Thermally annealed polyimide-based mixed matrix membrane containing ZIF-67 decorated porous graphene oxide nanosheets with enhanced propylene/propane selectivity. *J. Membr. Sci.* **603**, 118019 (2020).
43. S. Park, H.-K. Jeong, In-situ linker doping as an effective means to tune zeolitic-imidazolate framework-8 (ZIF-8) fillers in mixed-matrix membranes for propylene/propane separation. *J. Membr. Sci.* **596**, 117689 (2020).
44. J. Liu, Y. Xiao, T.-S. Chung, Flexible thermally treated 3D PIM-CD molecular sieve membranes exceeding the upper bound line for propylene/propane separation. *J. Mater. Chem. A* **5**, 4583–4595 (2017).
45. C. Zhang, R. P. Lively, K. Zhang, J. R. Johnson, O. Karvan, W. J. Koros, Unexpected molecular sieving properties of zeolitic imidazolate framework-8. *J. Phys. Chem. Lett.* **3**, 2130–2134 (2012).
46. L. Sheng, C. Wang, F. Yang, L. Xiang, X. Huang, J. Yu, L. Zhang, Y. Pan, Y. Li, Enhanced C_3H_6/C_3H_8 separation performance on MOF membranes through blocking defects and hindering framework flexibility by silicone rubber coating. *Chem. Commun.* **53**, 7760–7763 (2017).
47. E. Shamsaei, X. Lin, Z.-X. Low, Z. Abbasi, Y. Hu, J. Z. Liu, H. Wang, Aqueous phase synthesis of ZIF-8 membrane with controllable location on an asymmetrically porous polymer substrate. *ACS Appl. Mater. Interfaces* **8**, 6236–6244 (2016).
48. Y. Pan, W. Liu, Y. Zhao, C. Wang, Z. Lai, Improved ZIF-8 membrane: Effect of activation procedure and determination of diffusivities of light hydrocarbons. *J. Membr. Sci.* **493**, 88–96 (2015).
49. H. T. Kwon, H.-K. Jeong, Improving propylene/propane separation performance of zeolitic-imidazolate framework ZIF-8 Membranes. *Chem. Eng. Sci.* **124**, 20–26 (2015).
50. D. Liu, X. Ma, H. Xi, Y. Lin, Gas transport properties and propylene/propane separation characteristics of ZIF-8 membranes. *J. Membr. Sci.* **451**, 85–93 (2014).
51. D. Fairen-Jimenez, S. Moggach, M. Wharmby, P. Wright, S. Parsons, T. Duren, Opening the gate: Framework flexibility in ZIF-8 explored by experiments and simulations. *J. Am. Chem. Soc.* **133**, 8900–8902 (2011).
52. K. Li, D. H. Olson, J. Seidel, T. J. Emge, H. Gong, H. Zeng, J. Li, Zeolitic imidazolate frameworks for kinetic separation of propane and propene. *J. Am. Chem. Soc.* **131**, 10368–10369 (2009).
53. E. Cussler, Membranes containing selective flakes. *J. Membr. Sci.* **52**, 275–288 (1990).
54. J. A. Sheffel, M. Tsapatsis, A model for the performance of microporous mixed matrix membranes with oriented selective flakes. *J. Membr. Sci.* **295**, 50–70 (2007).
55. J. A. Sheffel, M. Tsapatsis, A semi-empirical approach for predicting the performance of mixed matrix membranes containing selective flakes. *J. Membr. Sci.* **326**, 595–607 (2009).
56. M. Shete, P. Kumar, J. E. Bachman, X. Ma, Z. P. Smith, W. Xu, K. A. Mkhoyan, J. R. Long, M. Tsapatsis, On the direct synthesis of Cu(BDC) MOF nanosheets and their performance in mixed matrix membranes. *J. Membr. Sci.* **549**, 312–320 (2018).
57. J. Winarta, A. Meshram, F. Zhu, R. Li, H. Jafar, K. Parmar, J. Liu, B. Mu, Metal–organic framework-based mixed-matrix membranes for gas separation: An overview. *J. Polym. Sci.* **58**, 2518–2546 (2020).
58. R. Lin, B. V. Hernandez, L. Ge, Z. Zhu, Metal organic framework based mixed matrix membranes: An overview on filler/polymer interfaces. *J. Mater. Chem. A* **6**, 293–312 (2018).
59. Y. Katayama, K. C. Bentz, S. M. Cohen, Defect-free MOF-based mixed-matrix membranes obtained by corona cross-linking. *ACS Appl. Mater. Interfaces* **11**, 13029–13037 (2019).
60. J. Yu, C. Wang, L. Xiang, Y. Xu, Y. Pan, Enhanced C_3H_6/C_3H_8 separation performance in poly(vinyl acetate) membrane blended with ZIF-8 nanocrystals. *Chem. Eng. Sci.* **179**, 1–12 (2018).
61. M. J. Lee, M. R. A. Hamid, J. Lee, J. S. Kim, Y. M. Lee, H.-K. Jeong, Ultrathin zeolitic-imidazolate framework ZIF-8 membranes on polymeric hollow fibers for propylene/propane separation. *J. Membr. Sci.* **559**, 28–34 (2018).
62. J. H. Kim, W. Koros, D. Paul, Physical aging of thin 6FDA-based polyimide membranes containing carboxyl acid groups. Part II. Optical properties. *Polymer* **47**, 3104–3111 (2006).
63. J. C. Tan, T. D. Bennett, A. K. Cheetham, Chemical structure, network topology, and porosity effects on the mechanical properties of zeolitic imidazolate frameworks. *Proc. Natl. Acad. Sci. U.S.A.* **107**, 9938–9943 (2010).
64. J. H. Shin, M.-Y. Kan, J.-W. Oh, H. J. Yu, L.-C. Lin, J.-H. Kim, D.-Y. Kang, J. S. Lee, Solubility selectivity-enhanced SIFSIX-3-Ni-containing mixed matrix membranes for improved CO_2/CH_4 separation efficiency. *J. Membr. Sci.* **633**, 119390 (2021).
65. K. Bowden, Acidity functions for strongly basic solutions. *Chem. Rev.* **66**, 119–131 (1966).
66. Y. Marcus, The properties of organic liquids that are relevant to their use as solvating solvents. *Chem. Soc. Rev.* **22**, 409–416 (1993).

Acknowledgments
Funding: This research was supported by the National Research Foundation of Korea (NRF) grant funded by the Korean government (MSIT) (NRF-2020R1C1C1003289 and NRF-2021M3H4A3A01049728). **Author contributions:** Conceptualization: D.W.K. Methodology: O.K., M.K., and E.C. Investigation: O.K., M.K., E.C., J.H.B., S.Y., J.C.W., Y.H.K., J.H.S., J.S.L. Visualization: O.K. and M.K. Supervision: D.W.K. Writing, original draft: O.K. and M.K. Writing, review and editing: O.K., M.K., and D.W.K. **Competing interests:** The authors declare that they have no competing interests. **Data and materials availability:** All data needed to evaluate the conclusions in the paper are present in the paper and/or the Supplementary Materials.

Submitted 29 July 2021
Accepted 10 November 2021
Published 5 January 2022
10.1126/sciadv.abl6841